



Size-dependent electron injection over sensitized semiconductor heterojunctions for enhanced photocatalytic hydrogen production

Wenkai Xu ^{a,b}, Jiansong Wang ^{a,c}, Hui Yu ^{a,b}, Peng Liu ^{a,c}, Gui-Rong Zhang ^{a,c,*},
Hongliang Huang ^{a,c,*}, Donghai Mei ^{a,b,c,d,*}

^a State Key Laboratory of Separation Membranes and Membrane Processes, Tiangong University, Tianjin 300387, PR China

^b School of Materials Science and Engineering, Tiangong University, Tianjin 300387, PR China

^c School of Chemical Engineering and Technology, Tiangong University, Tianjin 300387, PR China

^d School of Environmental Science and Engineering, Tiangong University, Tianjin 300387, PR China



ARTICLE INFO

Keywords:

CdS/Cd-TCPP

Heterojunction

Size effect

Electron injection

Photocatalytic H₂ evolution

ABSTRACT

Mechanistic understanding of the effect of electron transfer rate across the semiconductor heterojunction interface on its photocatalytic activity remains elusive. Herein, a series of sensitized semiconductor heterojunctions consisting of monodisperse CdS quantum dots (QDs) with controllable sizes range of 2.2–6.5 nm and cadmium tetrakis(4-carboxyphenyl)porphyrin (Cd-TCPP) nanosheets are constructed through partial sulfidation strategy. The in situ resultant CdS/Cd-TCPP composites exhibit size-dependent photocatalytic hydrogen evolution reaction (HER) activity with the highest activity of 3150 $\mu\text{mol}\cdot\text{h}^{-1}\cdot\text{g}^{-1}$ obtained at a medium CdS QD size of 4.8 nm. It is demonstrated that the interfacial electron transfer rate and the corresponding photocatalytic HER activity can be regulated by tuning the CdS QD size that determines the conduction band position of CdS relative to Cd-TCPP. This work provides a new strategy that rationally controls the interfacial electron transfer rate for developing highly efficient photocatalysts.

1. Introduction

Sunlight is the most abundant, clean and inexhaustible energy source on Earth. However, its diffuse and intermittent nature makes it difficult to use directly [1]. Among various technologies for solar energy utilization, photocatalytic hydrogen production could be the ultimate solution for the future energy crisis and environmental pollution issues [2–4]. Nevertheless, its practical realization requires stable, efficient and inexpensive semiconductor photocatalysts [5]. Various semiconductors such as TiO₂ [6,7], g-C₃N₄ [8,9], and CdS [10,11], have been explored for photocatalytic hydrogen production. Among them, CdS has been extensively studied as an ideal prototype due to its narrow bandgap (2.4 eV) and suitable conduction band (CB) position, allowing it to take full advantage of the visible-light for proton reduction reactions [12–14]. While the rapid recombination of photogenerated electron-hole, sluggish charge migration and severe photocorrosion greatly hinder further improvement of the photocatalytic efficiency of CdS [15].

In the past decades, many strategies such as suitable textural design

[16], doping [17], and designing proper heterojunctions [18], have been attempted to overcome these limitations. Among these, the construction of a proper semiconductor heterojunction, where electron transport is the basic process, has attracted tremendous attention due to its excellent light-harvesting ability, high charge separation efficiency, fast reaction kinetics and long-term stability [19–22]. Much effort has been devoted to design and fabricate various types of heterojunctions for exploring the heterojunction formation mechanism and the separation efficiency of photogenerated electrons and holes [23–25]. Only very few studies have focused on the rational regulation of the electron transfer rate across the heterojunction interface, which plays an essential role in determining the photocatalytic activity, especially for the photocatalytic hydrogen evolution reaction (HER) [26,27]. For example, it has been reported that chemically deposited CdS and CdSe QDs on TiO₂ [28], SnO₂ [29], and ZnO [30] surfaces are capable of injecting excited electrons and generating photocurrent under visible-light irradiation. Furthermore, QDs can exhibit unique quantum confinement effects, in this case, the charge carriers become spatially confined so that the energy of excitation is increased [31,32]. Inspired by these, one can readily

* Corresponding authors at: State Key Laboratory of Separation Membranes and Membrane Processes, Tiangong University, Tianjin 300387, PR China.

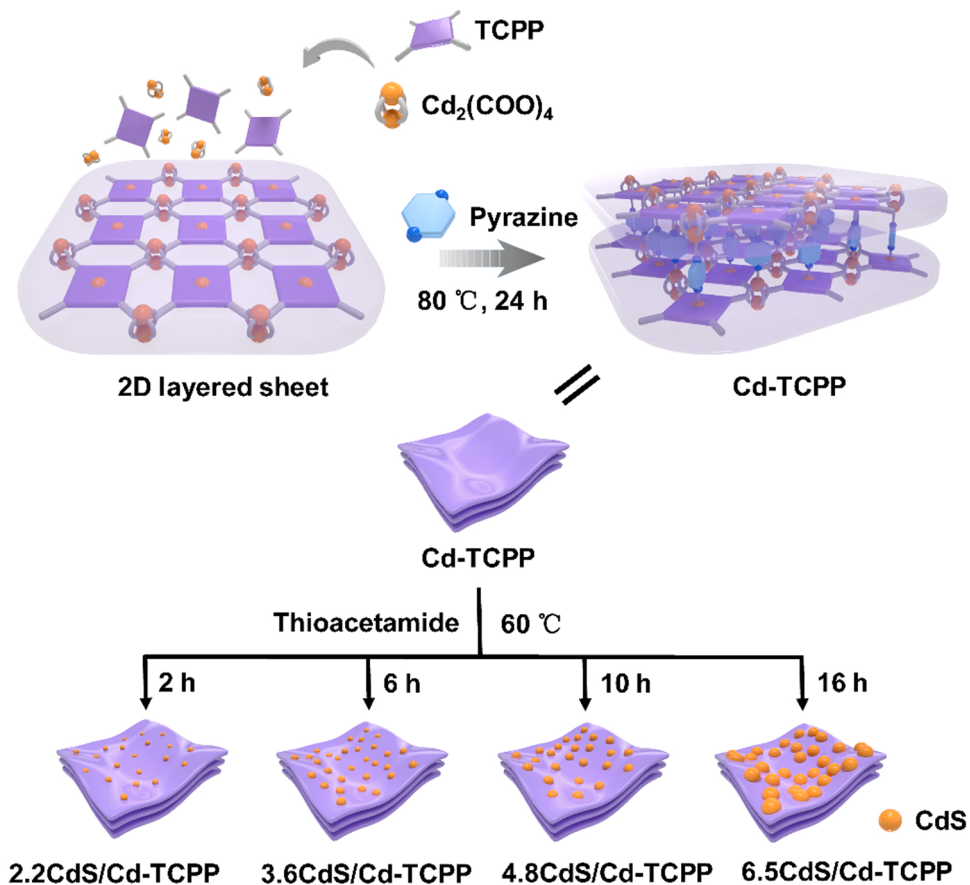
E-mail addresses: grzhang@tiangong.edu.cn (G.-R. Zhang), huanghongliang@tiangong.edu.cn (H. Huang), dhmei@tiangong.edu.cn (D. Mei).

tune the photoelectrochemical response and photoconversion efficiency in solar cells by controlling the size of QDs [33,34].

Traditionally, CdS QDs are synthesized using the colloidal method, and the QD sizes can be controlled by varying the capping agent (e.g., oleic acid (OA)) or its concentration [35,36], followed by a post-deposition procedure to obtain a heterojunction structured photocatalyst [37]. Nevertheless, it is a nontrivial task to remove the capping agent thereafter, which may compromise the photocatalytic performance of the CdS QDs [38]. Moreover, the post-deposition procedure is not favorable for the formation of an intimate contact interface within the heterojunction structure, which may lead to an increased charge transfer resistance [39,40]. Therefore, exploring the effect of CdS QDs size on the charge transfer behavior between the heterojunction interface faces two challenges: precise control of CdS QDs size and exclusion of the negative influence of the capping agent.

Metal-organic frameworks (MOFs), a novel class of porous crystals with diverse and tailorabile structures and functionalities, which are formed by assembly through coordination bonds between metal ions or clusters and functionalized organic linkers [41]. MOFs have been proven to be ideal templates for the preparation of target metal sulfide materials with controllable morphology and size [42,43]. Bearing these aspects in mind, herein, we report the first successful attempt to regulate the interfacial electron transfer rate as well as the photocatalytic HER activity by tuning the size of CdS QDs. In this work, the capping agent-free CdS QDs with narrow size distribution integrated with ultrathin 2D MOF nanosheets (NSs) are synthesized via in situ partial sulfidation of cadmium tetrakis(4-carboxyphenyl)porphyrin (Cd-TCPP), which is composed of $\text{Cd}_2(\text{COO})_4$ cluster nodes and photoresponsive metalloporphyrin ligands. In contrast to other carboxylate chelating groups (e.g. terephthalic acid) in the conventional MOF photocatalysts, the porphyrin groups in this work possess a larger π -conjugation system and

cause higher π -d orbital overlaps with metal nodes, which dramatically accelerates the ligand-to-node electron transfer and effectively suppresses the charge recombination, offering sufficient electrons for the photocatalytic reduction process [44–46]. The resultant heterojunction composites are denoted as $x\text{CdS}/\text{Cd-TCPP}$, where x represents the average CdS QD sizes ($x = 2.2, 3.6, 4.8$ and 6.5 nm) (As shown in **Scheme 1**). Compared with the pristine Cd-TCPP and pure CdS, the as-synthesized CdS/Cd-TCPP heterojunction photocatalysts show robust and superior performance toward the photocatalytic HER. The $4.8\text{CdS}/\text{Cd-TCPP}$ NSs exhibit the highest H_2 production rate of $3150\text{ }\mu\text{mol}\cdot\text{h}^{-1}\cdot\text{g}^{-1}$ without any cocatalysts, which is almost 5 times higher than that of CdS alone ($660\text{ }\mu\text{mol}\cdot\text{h}^{-1}\cdot\text{g}^{-1}$). Comprehensive characterizations including *in situ* irradiated X-ray photoelectron spectroscopy (ISI-XPS), cyclic voltammetry (CV), electron paramagnetic resonance (EPR), transient photocurrent response (TPR), Mott-Schottky (M-S) and transient-state photoluminescence (TRPL) spectroscopy tests unambiguously demonstrate that the electron transfer rate across the CdS/Cd-TCPP heterojunction interface depends on the relative CB position of CdS with respect to Cd-TCPP. This electron injection rate can be regulated by tuning the size of CdS QDs. Specifically, larger CdS QDs featuring a lower CB position are in principle more favorable for the electron transfer from Cd-TCPP to CdS via the so-called hot electron injection mechanism. We believe that these new findings will enrich our knowledge of heterojunction photocatalysts and provide a promising strategy for designing efficient photocatalysts for the solar-to-chemical energy conversion processes.



Scheme 1. Schematic illustration for the preparation of Cd-TCPP NSs and CdS/Cd-TCPP composite NSs.

2. Experimental section

2.1. Reagents

Cadmium nitrate tetrahydrate ($\text{Cd}(\text{NO}_3)_2 \cdot 4\text{H}_2\text{O}$, $\geq 98.5\%$) and thiocetamide (TAA, $>99\%$) were purchased from Alfa Aesar. Polyvinylpyrrolidone (PVP, $M_w = 40,000$) was purchased from Tokyo Chemical Industry Co., Ltd. Pyrazine (PY, $\geq 99\%$) and TCPP were purchased from Sigma-Aldrich. 1-octadecene (ODE, 95%), cadmium oxide (CdO , 99.99%), OA ($\geq 99\%$) and sulfur powder (99%) were purchased from Aladdin Industrial Corporation. N,N'-dimethylformamide (DMF, 99.8%), anhydrous ethanol (EtOH), acetonitrile and triethanolamine (TEOA) were purchased from Sinopharm Chemical Reagent Co., Ltd. All reagents are analytical grade and without additional purification. The deionized water was purified from Milli-Q System and used in all experiments.

2.2. Synthesis of Cd-TCPP

2D Cd-TCPP nanosheets were prepared by a hydrothermal method based on the previously reported procedure [47]. Briefly, $\text{Cd}(\text{NO}_3)_2 \cdot 4\text{H}_2\text{O}$ (0.015 mmol), PY (0.01 mmol) and PVP (0.5 mol) were dissolved in 12 mL of the mixture of DMF (9 mL) and EtOH (3 mL) in a 20 mL capped vial. The TCPP (0.005 mmol), dissolved in 4 mL of the mixture of DMF (3 mL) and EtOH (1 mL), was added dropwise into the aforementioned vial under stirred magnetically at room temperature, and the mixed solution was sonicated for 30 min. Then the vial was placed in an oven at 80°C for 24 h. After cooling down to the room temperature, the products were washed three times with EtOH and collected by centrifuging at 8000 rpm for 10 min. Finally, the dark green Cd-TCPP nanosheets were obtained.

2.3. Synthesis of CdS/Cd-TCPP

CdS/Cd-TCPP composite nanosheets were prepared via a facile partially sulfidation strategy based on the previously reported procedure with some modifications [43,48]. The total volume of the reaction solution was fixed at 16 mL, containing Cd-TCPP nanosheets (1 mg/mL, 4 mL), TAA (1 mg/mL, 4 mL) and EtOH (8 mL). The reaction vial was heated to 60°C and then kept for 2–16 h. The setting of reaction time with 2, 6, 10 and 16 h could result in CdS QDs with sizes of 2.2, 3.6, 4.8 and 6.5 nm confined on the surface of 2D Cd-TCPP nanosheets. The resulting composite nanosheets were washed three times with EtOH and collected by centrifuging at 8000 rpm for 10 min. The products were denoted as 2.2CdS/Cd-TCPP, 3.6CdS/Cd-TCPP, 4.8CdS/Cd-TCPP and 6.5CdS/Cd-TCPP, respectively.

2.4. Synthesis of CdS QDs

CdS QDs were synthesized by the typical hot-injection method [49]. The size of CdS QDs was regulated by adjusting the concentration of organic ligand and the temperature. In brief, a mixture of ODE (36 mL), CdO (3 mmol) and OA was heated to 280°C under argon atmosphere. The uses of OA with volumes of 3, 5, 10, 18 and 25 mL could result in CdS QDs with sizes of 3.3, 4.5, 5.4, 6.2 and 8.1 nm, respectively. A solution of sulphur (1.5 mmol) in ODE (10 mL) was swiftly injected into this hot solution and the mixture was cooled down to a specified temperature (220°C for 3.3 and 4.5 nm CdS QDs, 240°C for 5.4, 6.2 and 8.1 nm CdS QDs). The solution was maintained at that temperature for 1 h to allow the growth of CdS QDs. After cooled down to room temperature, the resulting CdS QDs with different particle sizes were purified three times with acetone and EtOH. The purified CdS QDs were redispersed in 20 mL chloroform for further use.

2.5. Characterization methods

Powder X-ray diffraction (PXRD) patterns were collected from a BRUKER D2 PHASER X-ray diffractometer equipped with graphite mono-chromatized Cu K radiation ($\lambda = 1.54056 \text{ \AA}$) at 30 kV and 10 mA. High-resolution transmission electron microscopy (HRTEM) images were obtained using a JEOL JEM-2100 F. A JEM-ARM200F TEM/STEM with a spherical aberration corrector working at 300 kV recorded the high-angle annular dark-field scanning transmission electron microscopy (HAADF-STEM), selected area electron diffraction (SAED) and energy dispersive spectroscopy (EDS) images. Fourier transform infrared (FT-IR) spectra were recorded on a Thermo Fisher Nicolet iS50 spectrophotometer. UV-visible diffuse reflectance spectra (UV-vis DRS) were measured on a UH4150 Ultraviolet-Visible-Near Infrared Spectrophotometer. Surface chemical state of the prepared samples was determined via XPS characterization using JPS-9010MC (JEOL, Japan) with an Al K α radiation hemispherical electron energy analyzer. The binding energies were referenced to the adventitious C1s peak at 284.8 eV. Meanwhile, a $\lambda \geq 420 \text{ nm}$ visible-light was placed ca. 20 cm away from the prepared samples during the ISI-XPS characterization to investigate the electron density changes. Inductively coupled plasma optical emission spectrometer (ICP-OES) results were obtained by a NexION 350 (Perkin Elmer) machine. EPR spectra were conducted on a Bruker A300 spectrometer. The steady-state PL emission spectra were obtained over a LS-55 fluorescence spectrometer made by PerkinElmer. Temperature-dependent PL spectra were acquired by Hitachi F-7800 fluorescence spectrophotometer equipped with low temperature accessory JANIS VPF-100. Element analyses (EA) were performed on a vario EI cube. Atomic force microscopy (AFM) images were obtained on a commercial atomic force microscope instrument (Dimension ICON with Nanoscope V controller, Bruker, USA).

2.6. Evaluation of photocatalytic activity

The photocatalytic hydrogen evolution experiments were carried out under visible-light irradiation. Before each test, 30 mg photocatalyst was dispersed in 30 mL acetonitrile and 10 mL deionized water with 10 mL TEOA as a sacrificial reagent, which leads to the formation of a homogeneous suspension with fine catalyst particles. The reactions were conducted using a photocatalytic H_2 production system (CEL-PAEM-D8) furnished by Beijing China Education Au-light Co., Ltd. The visible-light source was a 300 W xenon lamp equipped with a 420 nm cut off filter. The temperature of the reactant solution was maintained at 6°C by a flow of cooling water during the photocatalytic reaction. The amount of H_2 produced was determined every hour by using an on-line gas chromatography equipped with a TCD detector. The photocatalytic activity of various catalysts was evaluated by normalizing the hydrogen production rate to the mass of CdS.

2.7. Photoelectrochemical measurements

The photoelectrochemical tests were performed by a CHI760E electrochemical workstation (Chenhua Instrument, Shanghai). A standard three electrode system with the as-prepared catalysts dropped onto the pretreated FTO surfaces as the working electrode (FTO was ultrasonically washed three times with water, acetone and isopropanol, respectively.), the Ag/AgCl electrode (with saturated KCl as the internal solution) and the Pt wire were used as the reference and counter electrodes. 0.1 M Na_2SO_4 solution ($\text{pH}=7$) was used as the electrolyte and a 300 W xenon lamp equipped with a 420 nm UV cut off filter was used as light source. M-S test was recorded at a frequency of 1000 Hz. All the potential referred to $\text{E}(\text{Ag}/\text{AgCl})$ was transferred to the scale of standard hydrogen electrode (SHE) by the Nernst equation:

$$\text{E}(\text{SHE}) = \text{E}(\text{Ag}/\text{AgCl}) + 0.059 \text{ pH} + \text{E}^0(\text{Ag}/\text{AgCl}), \text{ where the } \text{E}^0(\text{Ag}/\text{AgCl}) \text{ is } 0.197 \text{ V vs. SHE.}$$

3. Results and discussion

3.1. Characterization of Cd-TCPP and CdS/Cd-TCPP

The Cd-TCPP NSs were first prepared using the surfactant-assisted solvothermal method [47]. On the Cd-TCPP NSs, each TCPP ligand is metallized by one cadmium ion and linked by four $\text{Cd}_2(\text{COO})_4$ paddle-wheel metal nodes, forming a “checkerboard-like” layered structure, which is further pillared by PY molecules in an AB stacking pattern (Scheme 1) [42,50]. The as-synthesized Cd-TCPP NSs were comprehensively characterized using TEM, HAADF-STEM, EDS elemental mapping, AFM and PXRD. Fig. 1 shows the representative TEM and HAADF-STEM images of pristine and sulfurized Cd-TCPP. The pristine Cd-TCPP exhibits a 2D nanosheet structure with a smooth surface (Fig. 1a,f). As revealed by AFM measurements, a typical 2D NS of Cd-TCPP has a lateral size of $3.0 \pm 0.5 \mu\text{m}$ (Fig. S1) and a thickness of $4.2 \pm 1.6 \text{ nm}$ (Fig. S2a-c). The EDS elemental mapping technique was employed to probe the chemical composition of the pristine Cd-TCPP. The characteristic signals including C, N, O and Cd elements can be clearly identified (Fig. S3). Moreover, the XRD patterns of the as-prepared Cd-TCPP NSs agree well with the simulated one (Fig. S4). All these characterization results clearly indicate that the Cd-TCPP NSs were successfully synthesized.

CdS/Cd-TCPP composites were prepared via in situ partial sulfidation of Cd-TCPP at 60°C using TAA as the sulfur source [43]. The representative TEM and STEM images of the as-synthesized CdS/Cd-TCPP composites are shown in Fig. 1. It can be seen that tiny nanoparticles (NPs) begin to appear after the sulfidation treatment for 2 h (Fig. 1b,g). The NPs have an average particle size of 2.2 nm, which are homogeneously distributed over the Cd-TCPP NSs without any localized aggregations. As the sulfidation time increases to 6, 10 and 16 h, the average size of NPs is enlarged to 3.6, 4.8 and 6.5 nm (Fig. 1h-j), respectively. While it is also observed that Cd-TCPP NSs maintain the 2D sheet-like morphology even for the sulfidation time of

16 h (Fig. S2d-f). The HRTEM was conducted to understand the crystalline structure of these NPs. Lattice fringes with a *d*-spacing of 0.33 nm identify the CdS (111) plane (Inset of Fig. 1d) [2]. This is further confirmed by the SAED measurement, which displays the characteristic patterns of CdS (111) and CdS (220) planes (Inset of Fig. 1e) [43]. Nevertheless, no distinct diffraction patterns of CdS can be observed in these CdS/Cd-TCPP composites, as reflected by their similar XRD patterns to that of the pristine Cd-TCPP (Fig. 2a). These results not only confirm the intact crystalline structure of Cd-TCPP after the sulfidation treatment, but also strongly imply the highly dispersed nature of ultrafine CdS NPs over the Cd-TCPP NSs. As expected, both the HAADF-STEM (Fig. 1k) and EDS elemental mapping characterizations (Fig. 1l-q) clearly show that CdS NPs are homogeneously distributed on Cd-TCPP without any particle agglomeration. However, we also note that the obtained CdS NPs exhibit severe agglomeration when the sulfidation time extends to 24 h (Fig. S5), as indicated by the diffraction peaks that are assigned to CdS (111) and CdS (220) planes can be distinguished at 27° and 44° (Fig. S6). At the same time, the characteristic diffraction peaks of Cd-TCPP are disappeared in the XRD patterns, implying that the long-time sulfidation has compromised the long-range ordered structure of Cd-TCPP. These results also imply that the sulfidation process may first occur at the nitrogen coordinated Cd sites (Cd-N_x) in the center of the porphyrin ring instead of the Cd-O_x clusters at metal nodes of the MOF. It appears that the sulfidation of the Cd-O_x clusters would only occur if Cd-N_x sites are close to being depleted, accompanied by a structural collapse, as is the case of CdS/Cd-TCPP prepared with a sulfidation time of 24 h.

FT-IR spectroscopy was used to probe the molecular structure of as-synthesized CdS/Cd-TCPP (Fig. 2b). First, it is noted that the characteristic IR bands of Cd-TCPP at 1380 cm^{-1} (C–N), 990 cm^{-1} (Cd–N), 820 – 740 cm^{-1} (C–H in the porphyrin ring), 1660 cm^{-1} (C=O) and 1300 – 1250 cm^{-1} (C–O) are maintained after the sulfidation, confirming the intact structure of Cd-TCPP [39,47]. Second, the stretching vibrational band of Cd–S (1060 cm^{-1}), which is observed in all

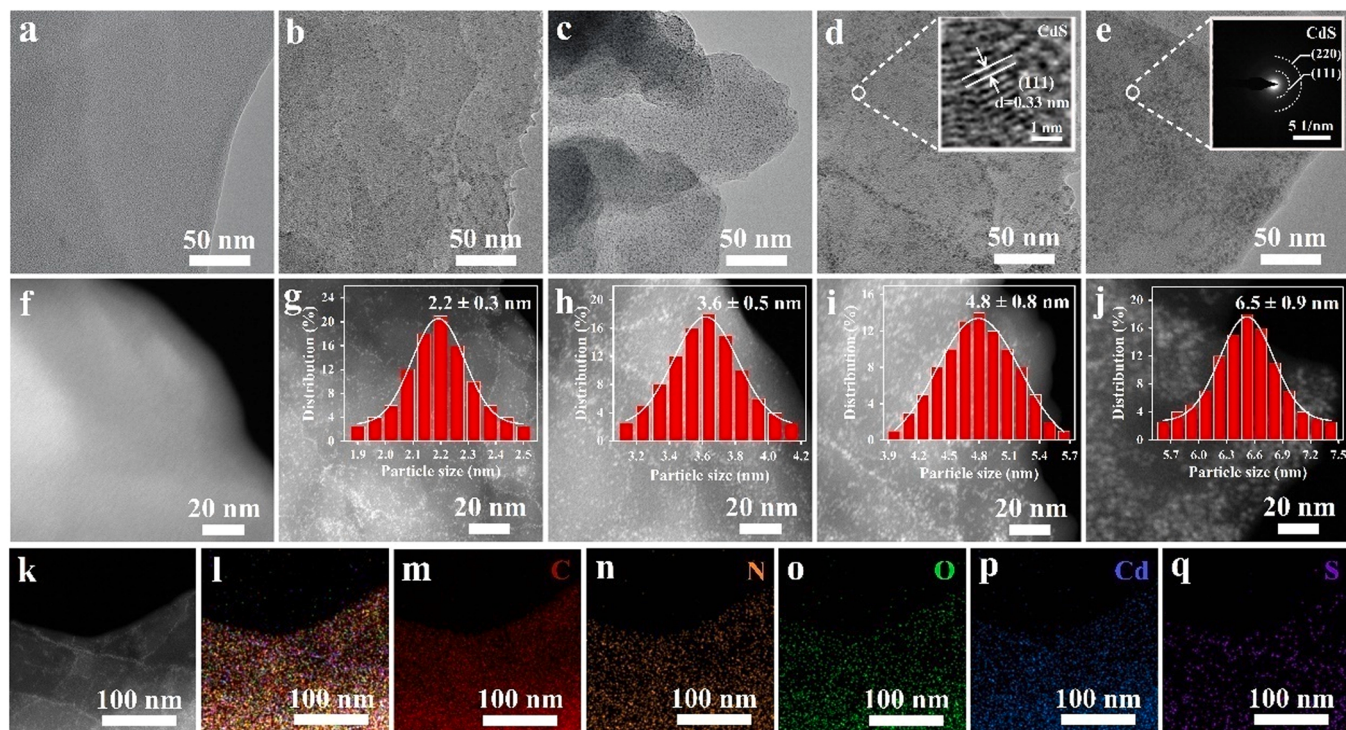


Fig. 1. (a-e) TEM, (f-j) HAADF-STEM images and corresponding particle size distributions of CdS QDs confined over Cd-TCPP NSs surface (Inset in Fig. g-j) of (a,f) the pristine Cd-TCPP NSs, (b,g) 2.2CdS/Cd-TCPP, (c,h) 3.6CdS/Cd-TCPP, (d,i) 4.8CdS/Cd-TCPP and (e,j) 6.5CdS/Cd-TCPP. HRTEM image (Inset of Fig. d) and SAED pattern (Inset of Fig. e) of single CdS QD. (k) HAADF-STEM and (l-q) corresponding EDS elemental mapping images of 4.8CdS/Cd-TCPP composite NSs.

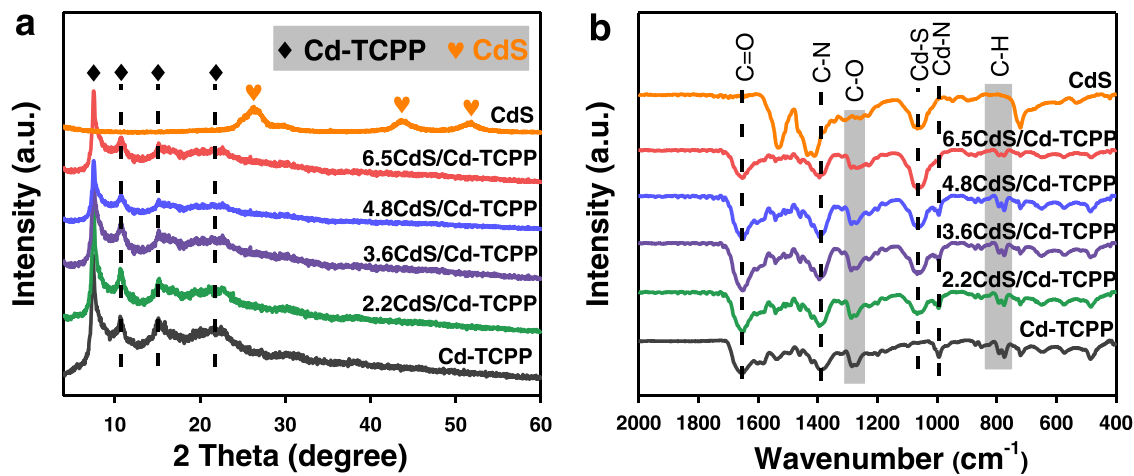


Fig. 2. (a) XRD patterns and (b) FT-IR spectra of CdS, Cd-TCPP and CdS/Cd-TCPP composites.

CdS/Cd-TCPP composites, becomes more pronounced as the sulfidation time increases (Fig. 2b). This is largely due to the increasing size of CdS with the sulfidation time [51]. A closer look of the FT-IR spectra of CdS/Cd-TCPP indicates the vibrational bands corresponding to C–N and Cd–N bonds are red-shifted, compared to those of the pristine Cd-TCPP (Fig. S7). This implies that there is a strong interaction between CdS and Cd-TCPP [52]. To further explore the interaction between CdS and Cd-TCPP in the as-prepared CdS/Cd-TCPP composites, high-resolution XPS spectra of S 2p, N 1s and O 1s in the CdS/Cd-TCPP composites were captured (Fig. S8). Interestingly, it is found that the binding energies (BEs) of S 2p in CdS/Cd-TCPP have negatively shifted with respect to the pure CdS. While the BEs of N 1s and O 1s in CdS/Cd-TCPP have positively shifted relative to those of the pristine Cd-TCPP. These results clearly suggest that the presence of CdS NPs has modified the electronic structure of Cd-TCPP and a charge transfer from Cd-TCPP NSs to CdS QDs occurs [53], which is consistent with the red-shifted vibrational bands in the FT-IR measurements.

The contents of CdS QDs in the composites of CdS-*y* wt% Cd-TCPP (*y* = 2.2, 3.2, 5.6 and 15.5) for 2.2CdS/Cd-TCPP, 3.6CdS/Cd-TCPP, 4.8CdS/Cd-TCPP and 6.5CdS/Cd-TCPP were measured using EA and ICP-OES (Table S1). It is worth noting that the total Cd content remains almost unchanged before and after sulfidation process (Fig. S9), suggesting that the sulfidation of Cd²⁺ proceeds in a stoichiometric manner. The leaching loss of Cd²⁺ during the washing procedure is negligible.

3.2. Photocatalytic HER activity and stability

Photocatalytic HER activity over CdS/Cd-TCPP catalysts was evaluated by monitoring the H₂ production rate under visible light ($\lambda \geq 420$ nm) irradiation. The reaction was performed in an aqueous solution containing TEOA as an electron donor. Control experiments (Fig. S10) show that no H₂ can be detected without catalyst or visible-light irradiation, indicating that the HER in this work is a photocatalytic process. Fig. 3a summarizes the H₂ production rates of CdS, Cd-TCPP and CdS/Cd-TCPP composites. For comparison, the performance of the physical mixture of CdS and Cd-TCPP is also included. It can be noticed that the pristine Cd-TCPP exhibits almost no activity toward the photocatalytic HER, while the reference CdS only show a moderate H₂ production rate of 660 $\mu\text{mol}\cdot\text{h}^{-1}\cdot\text{g}^{-1}$. In contrast, all of the CdS/Cd-TCPP composites show significantly enhanced HER activity, compared to either CdS or the physical mixture of CdS and TCPP (Fig. 3a). This indicates that the heterostructure of CdS/Cd-TCPP is essential for the superior photocatalytic HER activity. It is also noted that the HER activity shows a volcano-like dependence on the particle size of CdS. Specifically, as the CdS size increases from 2.2 to 4.8 nm, the H₂ production rate is increased gradually from 1780 $\mu\text{mol}\cdot\text{h}^{-1}\cdot\text{g}^{-1}$ on 2.2CdS/Cd-TCPP to 2370 $\mu\text{mol}\cdot\text{h}^{-1}\cdot\text{g}^{-1}$ on 3.6CdS/Cd-TCPP with a maximum of 3150 $\mu\text{mol}\cdot\text{h}^{-1}\cdot\text{g}^{-1}$ on 4.8CdS/Cd-TCPP. The maximum H₂ production rate is almost 5 times higher than that of the pure CdS (660 $\mu\text{mol}\cdot\text{h}^{-1}\cdot\text{g}^{-1}$). Further increasing the CdS particle size to 6.5 nm, however, leads to a decreased photocatalytic HER activity (2120 $\mu\text{mol}\cdot\text{h}^{-1}\cdot\text{g}^{-1}$).

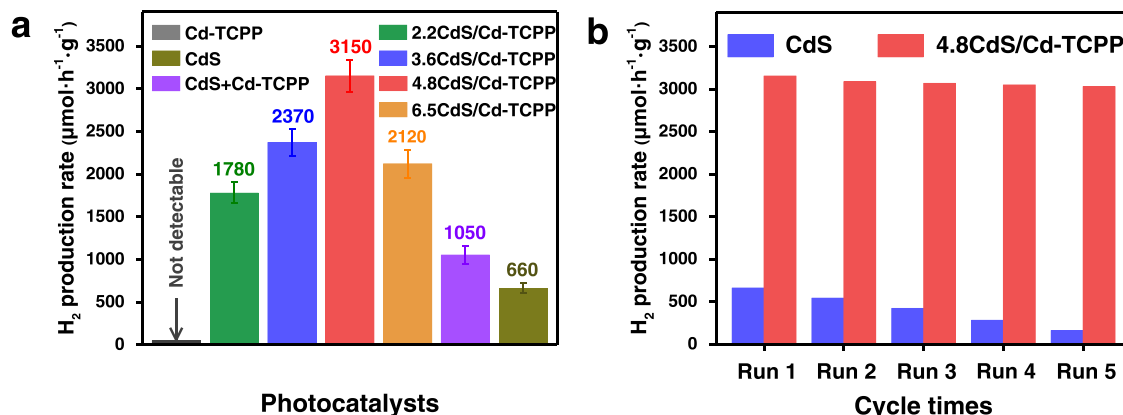


Fig. 3. (a) The photocatalytic hydrogen production rates of CdS, Cd-TCPP, physical mixture of CdS and Cd-TCPP (CdS+Cd-TCPP) and xCdS/Cd-TCPP (*x* = 2.2, 3.6, 4.8 and 6.5 nm) composites. (b) Photostability for the H₂ production of CdS and 4.8CdS/Cd-TCPP composites.

The photocatalytic stability of pure CdS and 4.8CdS/Cd-TCPP was investigated by performing uninterrupted photocatalytic H₂ production test for 30 h (Fig. S11). After five consecutive measurements (6 h per cycle), the 4.8CdS/Cd-TCPP composites still maintained a high H₂ production rate of 3025 $\mu\text{mol}\cdot\text{h}^{-1}\cdot\text{g}^{-1}$, which remains at least 96% of the initial value (Fig. 3b). No apparent change in either morphology or crystalline structure can be observed for the 4.8CdS/Cd-TCPP composites (Fig. S12). In sharp contrast, an obvious degradation can be observed on the pure CdS reference, which only keeps about 24% of the initial activity (160 $\mu\text{mol}\cdot\text{h}^{-1}\cdot\text{g}^{-1}$). The XRD patterns in Fig. S12a indicate that the crystallinity of pure CdS is weakened after the stability tests, which might be due to the photocorrosion. It can be clearly seen that CdS/Cd-TCPP composites exhibit much better photocatalytic stability than pristine CdS. Their superior photocatalytic stability may mainly derive from the following two aspects. (1) Porphyrin rings of Cd-TCPP feature abundant well distributed nitrogen sites which can serve as anchoring sites to stabilize CdS via nitrogen-metal bonds [54–57], and the strengthened interfacial interaction imparts CdS/Cd-TCPP composites improved structural stability. (2) The intimate 0D/2D heterojunction of CdS/Cd-TCPP reduces the diffusion length of photogenerated charge carriers, thus increasing the charge transfer/separation efficiency, which is also beneficial for improving the photocatalytic stability [58–62]. The excellent photocatalytic stability of CdS/Cd-TCPP composites demonstrates their practical applicability as high performance photocatalysts for the HER.

3.3. Optical properties and photogenerated carriers separation efficiency

The superior photocatalytic H₂ production performance and stability

of 4.8CdS/Cd-TCPP motivate us to explore the important role of binary heterojunction in the light harvesting, charge separation and transfer process. Hence, a series of characterization techniques including UV-vis DRS, steady-state PL spectroscopy, TRPL spectroscopy and electrochemical impedance spectroscopy (EIS) were performed. As shown in Fig. 4a, the photoresponse properties of the as-prepared samples were examined by UV-vis DRS. The pure CdS and pristine Cd-TCPP exhibit the absorption band edges at around 505 and 1160 nm, corresponding to the bandgaps of 2.66 (Fig. S16b) and 1.86 eV (Fig. S13b), respectively. The 4.8CdS/Cd-TCPP composites show an absorption edge of 1200 nm (Fig. 4a), which is comparable to that of the pristine Cd-TCPP. In contrast to the pure CdS, which has poor response to the visible-light, 4.8CdS/Cd-TCPP composites exhibit a much strong absorption of visible light (Fig. 4a). This can be attributed to the superior photo-absorption ability of the porphyrin units of Cd-TCPP under the visible-light irradiation [63,64]. To unveil the photogenerated carriers separation efficiency, the steady-state PL spectra has been measured under the excitation at 375 nm. Compared to the pure CdS and pristine Cd-TCPP, the peak intensity of the 4.8CdS/Cd-TCPP composites are remarkably diminished (Fig. 4b). This suggests that the recombination rate of electrons and holes in 4.8CdS/Cd-TCPP is obviously inhibited. Moreover, the TRPL spectra results (Fig. 4c) corroborate the longer average charge carrier lifetime ($\tau_{\text{ave}}=9.99$ ns) for 4.8CdS/Cd-TCPP than that of the pure CdS ($\tau_{\text{ave}}=7.74$ ns) (Table S2). The EIS Nyquist plot of 4.8CdS/Cd-TCPP (Fig. 4d) also displays a smaller arc radius than that of the pure CdS and pristine Cd-TCPP, indicative of its lower interfacial charge transfer resistance. These results clearly demonstrate the structural advantages of CdS/Cd-TCPP composites as a photocatalyst compared to the conventional CdS and pristine Cd-TCPP.

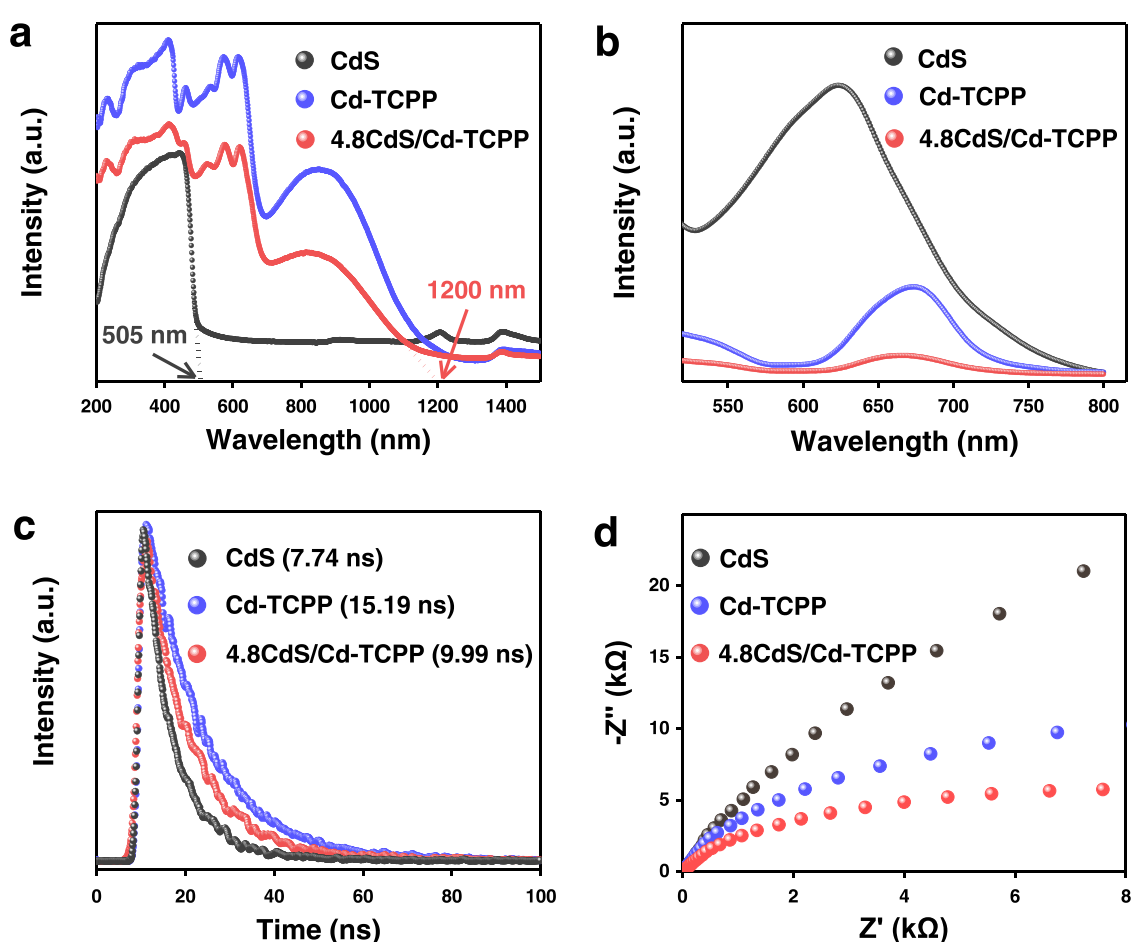


Fig. 4. (a) UV-vis DRS, (b) steady-state PL spectra, (c) TRPL spectra and (d) EIS plots of pure CdS, pristine Cd-TCPP and 4.8CdS/Cd-TCPP composites.

3.4. Proposed electron injection mechanism

To reveal the interfacial charge transfer pathway between CdS and Cd-TCPP in CdS/Cd-TCPP composites, ISI-XPS was performed (Fig. 5). Upon visible-light irradiation, there is a slightly negative shift (by -0.35 eV) in the S 2p binding energy, suggesting an increase in the electron density on the CdS QDs. Meanwhile, a slightly positive shift (by 0.3 eV) can also be observed in N 1s and O 1s, indicating a decrease in the electron density on the Cd-TCPP NSs. These binding energy shifts provide direct evidence of the charge carrier migration pathway across the CdS/Cd-TCPP interface [62,65]. In other words, the Cd-TCPP NSs are capable of injecting excited electrons into CdS QDs under visible-light irradiation, which is in good agreement with the electron injection mechanism.

It has been clearly observed that the size of CdS QDs significantly affects the performance of photocatalytic hydrogen production of CdS/Cd-TCPP composites. Hence, it is crucial to understand the size effect of QDs on the interfacial charge transfer between CdS QDs and Cd-TCPP NSs. First, CV was employed to explore the charge transfer behavior of various samples. The CV curves were recorded between 0.5 and 1.1 V (V vs. SHE) in 0.2 M Ar-saturated KCl solution containing 5 mM $K_3[Fe(CN)_6]$ at a scan rate of 10 mV/s under the visible-light irradiation. As shown in Fig. 6a, the reduction current density of -0.45 and -0.49 mA/cm 2 were observed at the pure CdS and pristine Cd-TCPP electrode, which can be attributed to the reduction reaction of $[Fe(CN)_6]^{3-}$ to form $[Fe(CN)_6]^{4-}$. As expected, the reduction current densities of CdS/Cd-TCPP composites show clear dependence on the size of CdS QDs. As the size of CdS QDs increases, the corresponding reduction current densities are gradually increased, as of -0.54 , -0.75 , -0.84 mA/cm 2 for 2.2 CdS/Cd-TCPP, 3.6 CdS/Cd-TCPP and 4.8 CdS/Cd-TCPP, respectively. While further increasing the size of CdS QDs to the 6.5 CdS/Cd-TCPP composites, the reduction current density decreases to -0.64 mA/cm 2 , suggesting that the photoelectrons for reduction reaction injected from Cd-TCPP NSs to 6.5 nm CdS QDs are pronouncedly decreased. As a result, corresponding to the photocatalytic activity, the reduction current density of CdS/Cd-TCPP composites also exhibits similar volcano dependence behavior on the CdS QDs sizes with the maximum value obtained on 4.8 CdS/Cd-TCPP composites.

The effect of CdS QDs sizes on the interfacial electron transfer rate was further explored employing the photocatalytic production of superoxide radicals ($\bullet O_2^-$) as a probe reaction. The rationality for this approach lies in that the semiconductors with the CB potential lower than the redox potential for $\bullet O_2^-$ formation (i.e., -0.33 V vs. SHE, pH=7) can produce the $\bullet O_2^-$ radical through the reaction of O_2 with the photogenerated electrons [66]. The produced $\bullet O_2^-$ was quantified using EPR analyses with $5,5$ -dimethyl- λ -pyrroline N-oxide (DMPO) as the trapping agent. First, under dark condition, no EPR signals can be detected on the investigated samples. In contrast, as shown in Fig. S14a-f, the EPR signals corresponding to DMPO- $\bullet O_2^-$ radicals can be clearly seen on pure CdS, pristine Cd-TCPP and CdS/Cd-TCPP

composites under visible-light irradiation. Second, different from those weak EPR signals of CdS and Cd-TCPP, four pronounced peaks were observed on CdS/Cd-TCPP composites, indicating that the latter exhibits an enhanced reduction capability due to photosensitized electron injection. Fig. 6b summarizes the $\bullet O_2^-$ generation rates over different samples, which are determined by the slope analysis of the plots of the EPR signal intensity against irradiation time (Fig. S14g) [41,67]. It can be observed that $\bullet O_2^-$ generation rates over all CdS/Cd-TCPP composites were faster than that over pure CdS and pristine Cd-TCPP. Again, the highest value was obtained on 4.8 CdS/Cd-TCPP, implying the fastest electron transfer rate among the investigated samples. These results clearly verify that the Cd-TCPP NSs are capable of injecting excited electrons into CdS QDs for generating more $\bullet O_2^-$ under visible-light irradiation. The photo-induced charge generation rate for the CdS/Cd-TCPP composites can be efficiently modulated by varying the CdS QDs size. Moreover, the TPR were also carried out under the visible-light irradiation. The photocurrent-time curves are in line with the EPR analyses (Fig. 6c). As expected, the photocurrent intensity of the CdS/Cd-TCPP composites are all obviously higher than that of the pure CdS and pristine Cd-TCPP. The 4.8 CdS/Cd-TCPP composites exhibit the highest photocurrent density under the identical measurement condition, confirming its high efficiency in generating photo-induced electrons.

To gain more insights into the size-dependent electron transfer/injection mechanism, attempts were made to quantify carrier concentration (N_d) by performing the M-S tests. The N_d can be calculated from the slope of M-S curves based on Eq. (1) [68]:

$$N_d = \frac{2}{e_0 \epsilon_0 \epsilon_r} \left(\frac{dC^{-2}}{dV} \right)^{-1} \quad (1)$$

where e_0 is the elemental charge (1.6×10^{-19} C), ϵ_0 is the permittivity of vacuum (8.85×10^{-14} F/m), ϵ_r is the dielectric constant of cadmium sulfide (~ 6) [69]. As shown in Fig. 6d, the pure CdS presents a much higher slope of M-S curve than that of the CdS/Cd-TCPP composites. The N_d was calculated to be 2.1×10^{19} cm $^{-3}$ for CdS (Fig. 6e). The moderate slopes can be seen from the M-S curves for the CdS/Cd-TCPP composites, suggesting the carrier concentration increases significantly by incorporating photosensitive Cd-TCPP NSs. The N_d was calculated to be 7.5×10^{19} , 2.6×10^{20} , 4.4×10^{20} and 1.7×10^{20} cm $^{-3}$ for 2.2 CdS/Cd-TCPP, 3.6 CdS/Cd-TCPP, 4.8 CdS/Cd-TCPP and 6.5 CdS/Cd-TCPP (Fig. 6e), respectively. This tendency is in good agreement with the photocatalytic hydrogen production performance, further confirming the important role of CdS QDs size in maximizing the photo-induced charge concentration.

The aforementioned ISI-XPS, CV, EPR, TPR characterizations and N_d calculation results clearly demonstrate the size-dependent photo-response properties of CdS/Cd-TCPP composites. The highest photo-response was obtained on the sample with the medium CdS QD size (i.e., 4.8 nm). Notably, the 4.8 CdS/Cd-TCPP composites also exhibit the

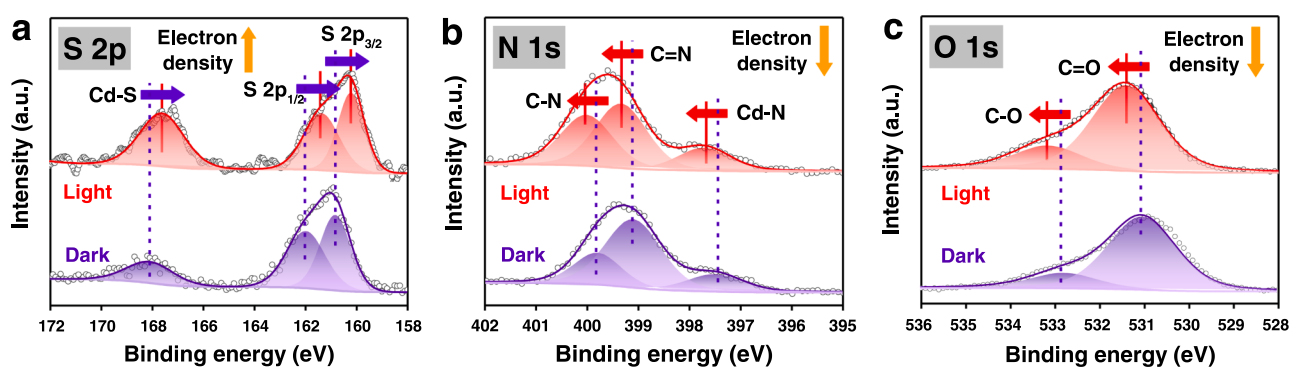


Fig. 5. High-resolution XPS for (a) S 2p, (b) N 1s and (c) O 1s of 4.8 CdS/Cd-TCPP composites in the dark or under visible-light irradiation.

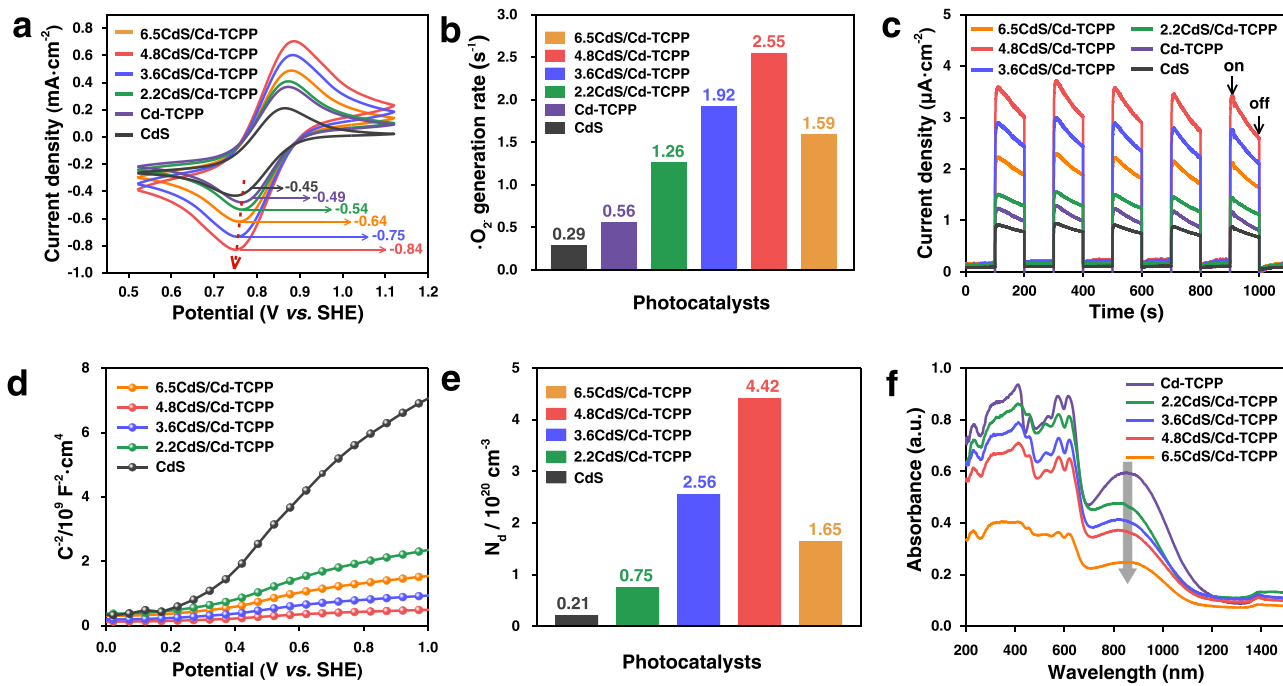


Fig. 6. (a) CV curves, (b) $\bullet\text{O}_2^-$ generation rate determined using EPR, (c) TPR, (d) the M-S curves, (e) carrier concentration and (f) UV-vis DRS of CdS, Cd-TCPP and χ CdS/Cd-TCPP ($\chi = 2.2, 3.6, 4.8$ and 6.5 nm) composites.

fastest hydrogen production rate among all investigated samples. Therefore, it is of significance to understand the size-dependent photoresponse properties of these CdS/Cd-TCPP composites before a fundamental structure-performance relationship can be established. Herein, the superior photocatalytic performance of CdS/Cd-TCPP composites may benefit largely from the synergistic interaction between CdS and Cd-TCPP. Specifically, 2D Cd-TCPP NSs are highly efficient for visible light harvesting (photosensitizer) [70], while CdS QDs are active for photocatalytic H_2 evolution (photocatalyst). The size-dependent photoresponse and photocatalytic behavior can thus be related to the photo-induced electron transfer (viz. hot electron injection) from Cd-TCPP NSs to CdS QDs. According to Marcus theory, the Gibbs free energy difference between the acceptor and donor systems serves as a driving force ($-\Delta G$) for the interfacial electron transfer [33,71,72]. As $-\Delta G$ increases, the rate of electron transfer increases, reaching a maximum when $-\Delta G$ equals the reorganization energy (i.e., when the Gibbs free energy of activation, $\Delta G^* = 0$) [73–75]. In the present study, the $-\Delta G$ for the electron injection from Cd-TCPP NSs to CdS QDs is expected to be determined by the energy difference between their CBs (Fig. 7b). Theoretically, CdS QDs with larger particle size would possess a smaller bandgap and a lower CB position [49]. To clarify this, CdS QDs with mean particle sizes ranging from 3.3 to 8.1 nm were synthesized

via a hot-injection method (Fig. S15) [49]. The bandgaps and CB positions of the resultant CdS QDs were determined on the basis of the UV-vis DRS and the M-S analyses. As displayed in Fig. 7a, when the average particle size increases from 3.3 to 8.1 nm, the bandgaps of CdS decreases from 2.72 to 2.40 eV, along with a lowered CB position (Fig. S16). These results verify that larger CdS QDs would in principle favor the hot electron injection due to their lowered CB position. Analogously, CdS/Cd-TCPP composites with larger CdS QD sizes are expected to be more photoresponsive (Fig. 7b). This speculation holds the validity for CdS/Cd-TCPP with CdS QD sizes ranging from 2.2 to 4.8 nm (Fig. 6a–e), which is also supported by TRPL. The excited Cd-TCPP deactivation was further analyzed by monitoring the PL emission decay. Fig. S17 shows the TRPL decay recorded with various CdS/Cd-TCPP composites. The average lifetime of Cd-TCPP emission decay is 15.19 ns (Fig. 4c, Table S2). When coupled with CdS, the average lifetimes decreased to 12.20, 10.95, 9.99 and 8.24 ns for 2.2CdS/Cd-TCPP, 3.6CdS/Cd-TCPP, 4.8CdS/Cd-TCPP and 6.5CdS/Cd-TCPP, respectively. The electron transfer rate constant can thus be estimated by assuming that the observed decrease in lifetime is due to the electron transfer to CdS according to Eq. (2) [33,34]:

$$k_{\text{et}} = \frac{1}{\tau_{(\text{CdS/Cd-TCPP})}} - \frac{1}{\tau_{(\text{Cd-TCPP})}} \quad (2)$$

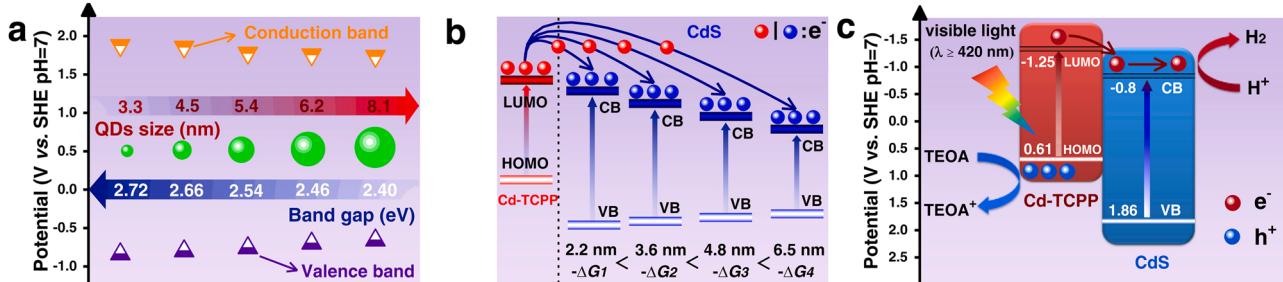


Fig. 7. (a) Size-dependent bandgaps and energy-band positions of CdS QDs with different sizes. (b) Schematic diagram of the CB position dependence of $-\Delta G$. The red and the blue spheres denote photoinduced electrons. (c) The exciton dissociation and transfer in the CdS/Cd-TCPP heterostructure under visible-light irradiation. The red and the blue spheres denote photoinduced electrons and holes, respectively.

Using the PL lifetime values listed in **Table 1**, we can obtain electron transfer rate constants of 1.61×10^7 , 2.55×10^7 and 3.43×10^7 for 2.2CdS/Cd-TCPP, 3.6CdS/Cd-TCPP and 4.8CdS/Cd-TCPP, respectively. This tendency is in good agreement with the N_d and photocatalytic hydrogen production performance. However, CdS/Cd-TCPP with the largest CdS QD size (i.e., 6.5 nm) exhibits worse photoresponse and lower photocatalytic activity despite its highest theoretical electron transfer rate, which deviates from the above speculation.

To resolve the above contradiction, UV-vis DRS measurements were performed on the CdS/Cd-TCPP composites. A closer examination of UV-vis DRS curves reveals that the light absorption intensity decreases with the increasing CdS QD size (Fig. 6f). This phenomenon might originate from the in situ conversion of the coordinated Cd centers in the Cd-TCPP into CdS, which has compromised the photosensitization efficiency of Cd-TCPP. Therefore, CdS/Cd-TCPP composites with larger CdS QD size, which were prepared with longer sulfidation time, always exhibit lower absorption intensity. This is especially the case for the 6.5CdS/Cd-TCPP composites, which were prepared by sulfidizing Cd-TCPP for 16 h. An abrupt drop in the absorption intensity is shown in Fig. 6f. On the basis of these results, it can be concluded that despite larger CdS QDs in principle are more favorable for the electron injection from Cd-TCPP to CdS, their synthesis process depletes more Cd centers in the Cd-TCPP substrate during the sulfidation. Therefore, the maximum photoresponse and photocatalytic activity are obtained on the sample with medium-sized CdS QDs (4.8CdS/Cd-TCPP), which would partially originate from the balance between favored hot electron injection and compromised photosensitivity due to the depletion of Cd centers in Cd-TCPP with enlarging CdS QDs.

The above results shed new light on the understanding the size-dependent electron injection mechanism in photocatalytic HER over CdS/Cd-TCPP catalysts, which is tentatively proposed as follows: the intimate contact between CdS and Cd-TCPP results in the formation of a type II (staggering type) heterojunction as displayed in Fig. 7c. Under the visible-light ($\lambda \geq 420$ nm) irradiation, the photoinduced electrons are injected from the CB of Cd-TCPP NSs to the CB of CdS QDs. Subsequently, these hot electrons migrate to the surface of CdS QDs, and combine with protons forming H_2 . Meanwhile, the photogenerated holes remain on the valence band (VB) of Cd-TCPP for the oxidation of TEOA into the oxidation products. Among various CdS/Cd-TCPP composites, the 4.8CdS/Cd-TCPP composites possessing a medium sized CdS and a favorable CB position can efficiently facilitate the hot electron injection process without triggering significant structural damage to the photosensitizer Cd-TCPP, thus exhibiting the maximum photocatalytic activity. These findings echo the importance of properly tailored heterostructures for fabricating high-performance photocatalysts.

4. Conclusions

In summary, we demonstrate that the interfacial electron transfer/injection rate as well as photocatalytic HER activity of CdS/Cd-TCPP heterojunction photocatalysts can be rationally regulated by tuning the size of CdS QDs. It is also disclosed that the driving force for the electron transfer/injection across the heterojunction interfaces stems from the energy gap between the CBs of CdS and Cd-TCPP. Comprehensive experimental characterizations reveal that CdS/Cd-TCPP composites with larger CdS QD sizes are more favorable for accepting the injected electrons from Cd-TCPP substrate due to their lower CB positions that increases the driving force of electron injection. However, the in situ synthesis of larger CdS QD sizes would have depleted more Cd centers from Cd-TCPP during the sulfidation process, thus compromising its photoresponse capability. Consequently, the best photocatalytic activity was obtained on the CdS/Cd-TCPP composites with a medium CdS QD size (i.e., 4.8 nm), which exhibit almost five times higher HER activity than that of the pure CdS. The new mechanistic insights into the size effect of CdS on the photocatalytic HER provided in this work would have an important impact on the rational design and development of

Table 1

Kinetic parameters of the Cd-TCPP PL emission decay analysis.

Sample	A_1	τ_1 (ns)	A_2	τ_2 (ns)	τ_{ave} (ns)	$k_{ef} \cdot 10^7$ s^{-1}
Cd-TCPP	601.50	15.26	85.32	14.64	15.19	
2.2CdS/Cd-TCPP	644.12	12.14	63.67	12.81	12.20	1.61
3.6CdS/Cd-TCPP	206.40	10.67	30.41	12.60	10.95	2.55
4.8CdS/Cd-TCPP	182.85	10.20	15.38	5.22	9.99	3.43

high-performance photocatalysts for efficient conversion of solar energy to hydrogen fuels and other useful chemicals.

CRediT authorship contribution statement

Wenkai Xu: Investigation, Methodology, Writing – original draft. **Jiansong Wang:** Investigation. **Hui Yu:** Investigation. **Peng Liu:** Investigation. **Hongliang Huang:** Writing – review & editing, Supervision. **Gui-Rong Zhang:** Writing – review & editing, Supervision. **Donghai Mei:** Conceptualization, Writing – review & editing, Supervision.

Declaration of Competing Interest

The authors declare that they have no known competing financial interests or personal relationships that could have appeared to influence the work reported in this paper.

Acknowledgements

This work is supported by the National Natural Science Foundation of China (No. 91961119). The authors are thankful to the Analytical & Testing Center of Tiangong University for the technical support in HRTEM and XPS measurements.

Appendix A. Supporting information

Supplementary data associated with this article can be found in the online version at [doi:10.1016/j.apcatb.2022.121218](https://doi.org/10.1016/j.apcatb.2022.121218).

References

- [1] X.N. Wang, F.L. Wang, Y.H. Sang, H. Liu, *Adv. Energy Mater.* 7 (2017) 1700473.
- [2] B.Y. Dai, J.J. Fang, Y.R. Yu, M.L. Sun, H.M. Huang, C.H. Lu, J.H. Kou, Y.J. Zhao, Z. Z. Xu, *Adv. Mater.* 32 (2020), 1906361.
- [3] G.Q. Han, Y.H. Jin, R.A. Burgess, N.E. Dickenson, X.M. Cao, Y.J. Sun, *J. Am. Chem. Soc.* 139 (2017) 15584–15587.
- [4] S. Hejazi, S. Mohajernia, B. Osuagwu, G. Zoppellaro, P. Andryskova, O. Tomanec, S. Kment, R. Zboril, P. Schmuki, *Adv. Mater.* 32 (2020), 1908505.
- [5] S.S. Chen, T. Takata, K. Domen, *Nat. Rev. Mater.* 2 (2017) 17050–17066.
- [6] H.L. Xiong, L.L. Wu, Y. Liu, T.N. Gao, K.Q. Li, Y. Long, R. Zhang, L. Zhang, Z. A. Qiao, Q.S. Huo, X. Ge, S.Y. Song, H.J. Zhang, *Adv. Energy Mater.* 9 (2019), 1901634.
- [7] H. Zhao, Z.Y. Hu, J. Liu, Y. Li, M. Wu, G.V. Tendeloo, B.L. Su, *Nano Energy* 47 (2018) 266–274.
- [8] X.J. She, J.J. Wu, H. Xu, J. Zhong, Y. Wang, Y.H. Song, K.Q. Nie, Y. Liu, Y.C. Yang, M.T.F. Rodrigues, R. Vajtai, J. Lou, D.L. Du, H.M. Li, P.M. Ajayan, *Adv. Energy Mater.* 7 (2017), 1700025.
- [9] L.H. Lin, H.H. Ou, Y.F. Zhang, X.C. Wang, *ACS Catal.* 6 (2016) 3921–3931.
- [10] P. Zhou, Q.H. Zhang, Z.K. Xu, Q.Y. Shang, L. Wang, Y.G. Chao, Y.J. Li, H. Chen, F. Lv, Q. Zhang, L. Gu, S.J. Guo, *Adv. Mater.* 32 (2020), 1904249.
- [11] X.M. Zhang, H.C. Liang, H.Z. Li, Y. Xia, X.H. Zhu, L. Peng, W. Zhang, L.L. Liu, T. C. Zhao, C.Y. Wang, Z.W. Zhao, C.T. Hung, M.M. Zagho, A. Elzathary, W. Li, D. Y. Zhao, *Angew. Chem. Int. Ed.* 59 (2020) 3287–3293.
- [12] J.Y. Li, Y.H. Li, M.Y. Qi, Q. Lin, Z.R. Tang, Y.J. Xu, *ACS Catal.* 10 (2020) 6262–6280.
- [13] C.M. Wolff, P.D. Frischmann, M. Schulze, B.J. Bohn, R. Wein, P. Livadas, M. T. Carlson, F. Jäckel, J. Feldmann, F. Würthner, J.K. Stolarczyk, *Nat. Energy* 3 (2018) 862–869.
- [14] W.K. Wei, Q.F. Tian, H.S. Sun, P. Liu, Y. Zheng, M.Z. Fan, J.D. Zhuang, *Appl. Catal. B* 260 (2020), 118153.

[15] L. Cheng, Q.J. Xiang, Y.L. Liao, H.W. Zhang, *Energy Environ. Sci.* 6 (2018) 1362–1391.

[16] L.H. Lin, Z.Y. Lin, J. Zhang, X. Cai, W. Lin, Z.Y. Yu, X.C. Wang, *Nat. Catal.* 3 (2020) 649–655.

[17] S.J. Qiu, Y.L. Shen, G.J. Wei, S. Yao, W. Xi, M. Shu, R. Si, M. Zhang, J.F. Zhu, C. H. An, *Appl. Catal. B* 259 (2019), 118036.

[18] Z.P. Li, W.X. Huang, J.X. Liu, K.L. Lv, Q. Li, *ACS Catal.* 11 (2021) 8510–8520.

[19] H.L. Wang, L.S. Zhang, Z.G. Chen, J.Q. Hu, S.J. Li, Z.H. Wang, J.S. Liu, X.C. Wang, *Chem. Soc. Rev.* 43 (2014) 5234–5244.

[20] Q.L. Xu, L.Y. Zhang, B. Cheng, J.J. Fan, J.G. Yu, *Chem* 6 (2020) 1543–1559.

[21] L. Yuan, Z.Y. Geng, J.K. Xu, F. Guo, C. Han, *Adv. Funct. Mater.* 31 (2021), 2101103.

[22] P. Zhou, J.G. Yu, M. Jaroniec, *Adv. Mater.* 26 (2014) 4920–4935.

[23] Y. Lu, X. Cheng, G. Tian, H. Zhao, L. He, J. Hu, S.M. Wu, Y. Dong, G.G. Chang, S. Lenaerts, S. Siffert, G.V. Tendeloo, Z.F. Li, L.L. Xu, X.Y. Yang, B.L. Su, *Nano Energy* 47 (2018) 8–17.

[24] B.C. Qiu, L.J. Cai, N. Zhang, X.M. Tao, Y. Chai, *Adv. Sci.* 7 (2020), 1903568.

[25] B.C. Qiu, Q.H. Zhu, M.M. Du, L.G. Fan, M.Y. Xing, J.L. Zhang, *Angew. Chem. Int. Ed.* 56 (2017) 2684–2688.

[26] R. Long, D. Casanova, W.H. Fang, O.V. Prezhdo, *J. Am. Chem. Soc.* 139 (2017) 2619–2629.

[27] H.F. Li, H. Li, S.N. Xun, J.L. Brédas, *Chem. Mater.* 32 (2020) 9228–9237.

[28] E.C. Hao, B. Yang, J.H. Zhang, X. Zhang, J.C. Shen, *J. Mater. Chem. B* (1998) 1327–1328.

[29] C. Nasr, S. Hotchandani, W.Y. Kim, R.H. Schmehl, P.V. Kamat, *J. Phys. Chem. B* 101 (1997) 7480–7487.

[30] S. Hotchandani, P.V. Kamat, *Chem. Phys. Lett.* 191 (1992) 320–326.

[31] Q. Guo, F. Liang, X.B. Li, Y.J. Gao, M.Y. Huang, Y. Wang, S.G. Xia, X.Y. Gao, Q. C. Gan, Z.S. Lin, C.H. Tung, L.Z. Wu, *Chem* 5 (2019) 2605–2616.

[32] X.B. Li, C.H. Tung, L.Z. Wu, *Nat. Rev. Chem.* 2 (2018) 160–173.

[33] A. Kongkanand, K. Tvrdy, K. Takechi, M. Kuno, P.V. Kamat, *J. Am. Chem. Soc.* 130 (2008) 4007–4015.

[34] K. Tvrdy, P.A. Frantsuzov, P.V. Kamat, *PNAS* 108 (2011) 29–34.

[35] A.P. Alivisatos, *Science* 271 (1996), 933–933.

[36] W.W. Yu, X.G. Peng, *Angew. Chem. Int. Ed.* 114 (2002) 2474–2477.

[37] M.Y. Qi, Y.H. Li, M. Anpo, Z.R. Tang, Y.J. Xu, *ACS Catal.* 10 (2020) 14327–14335.

[38] C.Y. Dong, C. Lian, S.C. Hu, Z.S. Deng, J.Q. Gong, M.D. Li, H.L. Liu, M.Y. Xing, J. L. Zhang, *Nat. Commun.* 9 (2018) 1252–1262.

[39] J.R. Ran, J.T. Qu, H.P. Zhang, T. Wen, H.L. Wang, S.M. Chen, L. Song, X.L. Zhang, L.Q. Jing, R.K. Zheng, S.Z. Qiao, *Adv. Energy Mater.* 9 (2019), 1803402.

[40] X.R. Gan, D.Y. Lei, R.Q. Ye, H.M. Zhao, K.Y. Wong, *Nano Res.* 14 (2020) 2003–2022.

[41] W.K. Xu, W.J. Xue, H.L. Huang, J.S. Wang, C.L. Zhong, D.H. Mei, *Appl. Catal. B* 291 (2021), 120129.

[42] F.F. Cao, M.T. Zhao, Y.F. Yu, B. Chen, Y. Huang, J. Yang, X.H. Cao, Q.P. Lu, X. Zhang, Z.C. Zhang, C.L. Tan, H. Zhang, *J. Am. Chem. Soc.* 138 (2016) 6924–6927.

[43] Q.P. Lu, M.T. Zhao, J.Z. Chen, B. Chen, C.L. Tan, X. Zhang, Y. Huang, J. Yang, F. F. Cao, Y.F. Yu, J.F. Ping, Z.C. Zhang, X.J. Wu, H. Zhang, *Small* 12 (2016) 4669–4674.

[44] Z.B. Fang, T.T. Liu, J.X. Liu, S.Y. Jin, X.P. Wu, X.Q. Gong, K.C. Wang, Q. Yin, T. F. Liu, R. Cao, H.C. Zhou, *J. Am. Chem. Soc.* 142 (2020) 12515–12523.

[45] M.L. Aubrey, B.M. Wiers, S.C. Andrews, T. Sakurai, S.E. Reyes-Lillo, S.M. Hamed, C.-J. Yu, L.E. Darago, J.A. Mason, J.-O. Baeg, F. Grandjean, G.J. Long, S. Seki, J. B. Neaton, P. Yang, J.R. Long, *Nat. Mater.* 17 (2018) 625–632.

[46] S.R. Ahrenholz, C.C. Epley, A.J. Morris, *J. Am. Chem. Soc.* 136 (2014) 2464–2472.

[47] M.T. Zhao, Y.X. Wang, Q.L. Ma, Y. Huang, X. Zhang, J.F. Ping, Z.C. Zhang, Q.P. Lu, Y.F. Yu, H. Xu, Y.L. Zhao, H. Zhang, *Adv. Mater.* 27 (2015) 7372–7378.

[48] K. Cho, S.H. Han, M.P. Suh, *Angew. Chem. Int. Ed.* 55 (2016) 15301–15305.

[49] X.J. Wu, X.T. Fan, S.J. Xie, J.C. Lin, J. Cheng, Q.H. Zhang, L.Y. Chen, Y. Wang, *Nat. Catal.* 1 (2018) 772–780.

[50] Y.X. Wang, M.T. Zhao, J.F. Ping, B. Chen, X.H. Cao, Y. Huang, C.L. Tan, Q.L. Ma, S. X. Wu, Y.F. Yu, Q.P. Lu, J.Z. Chen, W. Zhao, Y.B. Ying, H. Zhang, *Adv. Mater.* 28 (2016) 4149–4155.

[51] J. Fu, B.B. Chang, Y.L. Tian, F.N. Xi, X.P. Dong, *J. Mater. Chem. A* 1 (2013) 3083–3090.

[52] Z.Y. Zhang, K.C. Liu, Z.Q. Feng, Y.N. Bao, B. Dong, *Sci. Rep.* 6 (2016) 19221.

[53] Z.F. Jiang, W.M. Wan, H.M. Li, S.Q. Yuan, H.J. Zhao, P.K. Wong, *Adv. Mater.* 30 (2018), 1706108.

[54] F.C. Leng, H. Liu, M.L. Ding, Q.P. Lin, H.L. Jiang, *ACS Catal.* 8 (2018) 4583–4590.

[55] C. Cheng, B.W. He, J.J. Fan, B. Cheng, S.W. Cao, J.G. Yu, *Adv. Mater.* 33 (2021), 2100317.

[56] D.K. Wang, H. Zeng, X. Xiong, M.F. Wu, M.R. Xia, M.L. Xie, J.P. Zou, S.L. Luo, *Sci. Bull.* 65 (2020) 113–122.

[57] T.W. Deelen, C.H. Mejia, K.P. Jong, *Nat. Catal.* 2 (2019) 955–970.

[58] Y.Q. Sheng, W.L. Li, Y.F. Zhu, L.L. Zhang, *Appl. Catal. B* 298 (2021), 120585.

[59] H. Yang, C. Yang, N.N. Zhang, K.L. Mo, Q. Li, K.L. Lv, J.J. Fan, L.L. Wen, *Appl. Catal. B* 285 (2021), 119801.

[60] X.F. Li, X.F. Wu, S.W. Liu, Y.H. Li, J.J. Fan, K.L. Lv, *Chin. J. Catal.* 41 (2020) 1451–1467.

[61] R.N. Li, X.Y. Ou, L. Zhang, Z. Qi, C.S. Lu, J.J. Fan, K.L. Lv, *Chem. Commun.* 57 (2021) 10067–10070.

[62] P.F. Xia, S.W. Cao, B.C. Zhu, M.J. Liu, M.S. Shi, J.G. Yu, Y.F. Zhang, *Angew. Chem. Int. Ed.* 59 (2020) 5218–5225.

[63] T. He, S.M. Chen, B. Ni, Y. Gong, Z. Wu, L. Song, L. Gu, W.P. Hu, X. Wang, *Angew. Chem. Int. Ed.* 57 (2018) 3493–3498.

[64] H.Q. Xu, J.H. Hu, D.K. Wang, Z.H. Li, Q. Zhang, Y. Luo, S.H. Yu, H.L. Jiang, *J. Am. Chem. Soc.* 137 (2015) 13440–13443.

[65] J.X. Low, B.Z. Dai, T. Tong, C.J. Jiang, J.G. Yu, *Adv. Mater.* 31 (2019), 1802981.

[66] Y. Nosaka, A.Y. Nosaka, *Chem. Rev.* 117 (2017) 11302–11336.

[67] H. Li, J. Shang, Z.P. Yang, W.J. Shen, Z.H. Ai, L.Z. Zhang, *Environ. Sci. Technol.* 51 (2017) 5685–5694.

[68] Z.L. Wang, X. Mao, P. Chen, M. Xiao, S.A. Monny, S.C. Wang, M. Konarova, A. J. Du, L.Z. Wang, *Angew. Chem. Int. Ed.* 58 (2019) 1030–1034.

[69] I. Angeloni, W. Raja, R. Brescia, A. Polovitsyn, F.D. Donato, M. Canepa, G. Bertoni, R.P. Zaccaria, I. Moreels, *ACS Photonics* 3 (2016) 58–67.

[70] L. Wang, S.H. Duan, P.X. Jin, H.D. She, J.W. Huang, Z.Q. Lei, T.R. Zhang, Q. Z. Wang, *Appl. Catal. B* 239 (2018) 599–608.

[71] D.A. Gaal, J.T. Hupp, *J. Am. Chem. Soc.* 122 (2000) 10956–10963.

[72] P.V. Kamat, *Acc. Chem. Res.* 45 (2012) 1906–1915.

[73] I. Robel, M. Kuno, P.V. Kamat, *J. Am. Chem. Soc.* 129 (2007) 4136–4137.

[74] J.E. Huang, D. Stockwell, Z.Q. Huang, D.L. Mohler, T.Q. Lian, *J. Am. Chem. Soc.* 130 (2008) 5632–5633.

[75] J. Zhao, M.A. Holmes, F.E. Osterloh, *ACS Nano* 7 (2013) 4316–4325.